Self-Assembly of Hydroxyl Metal–Organic Polyhedra and Polymer into Cu-Based Hollow Spheres for Product-Selective CO_2 Electroreduction

Ru-Xin Yang, Yi-Rong Wang, Guang-Kuo Gao, Lin Chen, Yifa Chen,* Shun-Li Li,* and Ya-Qian Lan*

The electrochemical CO_2 reduction reaction (CO_2RR), an elegant solution to mitigate the greenhouse effect and produce high-value feedstock, has significant hurdles in selective production of target products. Herein, a series of Cu-based hollow spheres is synthesized through the self-assembly of hydroxyl metal–organic polyhedra and a polymer. The obtained materials with tunable morphology and compositions enable precise generation of varied products in a flow cell. Specifically, polymer-induced sol–gel (PISG)-3 shows 61.1% (-0.9 V, -143 mA cm^{-2}) Faradaic efficiency (FE) of C_2H_4 and negligible CH_4, higher than that of PISG-1 (FE$_{C_2H_4}$ 46.7%) with solid-sphere morphology. Interestingly, the products can be well tuned from C_2H_4 to CH_4 by introducing $CaCO_3$, along with increased hydrocarbon selectivity and CO_2 reduction efficiency. Notably, PISG-8 with modified composition displays drastically changed products (FE$_{CH_4}$ 55.8% and FE$_{C_2H_4}$ 22.2%, -162 mA cm^{-2}, -0.9 V). As certified by density functional theory calculations, $CaCO_3$ is proven to decrease the possibility for coexistence of two adjacent *CHO to restrain the dimerization process and enhance the CH_4 selectivity.

1. Introduction

The excessive emission of CO_2, mostly as a result of human activity, has increased exponentially during past decades and led to

Dr. R.-X. Yang, Dr. Y.-R. Wang, Dr. G.-K. Gao, Dr. L. Chen, Prof. Y. Chen, Prof. S.-L. Li, Prof. Y.-Q. Lan
Jiangsu Collaborative Innovation Centre of Biomedical Functional Materials
Jiangsu Key Laboratory of New Power Batteries
School of Chemistry and Materials Science
Nanjing Normal University
Nanjing 210023, P. R. China
E-mail: chyf927821@163.com; slli@njnu.edu.cn; yqlan@njnu.edu.cn, yqlan@m.scnu.edu.cn

Dr. G.-K. Gao, Prof. Y.-Q. Lan
School of Chemistry
South China Normal University
Guangzhou 510006, P. R. China

Prof. Y. Chen
Changzhou Institute of Innovation & Development
Nanjing Normal University
Nanjing 210023, P. R. China

The ORCID identification number(s) for the author(s) of this article can be found under https://doi.org/10.1002/sstr.202100012.

serious environmental issues, including the sea level rising, glaciers melting, land desertification, and more erratic weather patterns.[1] Converting CO_2 into fuels or value-added feedstocks, ideally if powered by renewable electricity, provides a promising avenue to mitigate greenhouse gas emissions and simultaneously close the carbon loop.[2–4] Specifically, the electrochemical CO_2 reduction reaction (CO_2RR) holds promise in conversion of thermodynamically stable and chemically inert CO_2 into products such as CO, formic acid, CH_4, C_2H_4, and ethanol when triggered by electricity, which might be an alternative to dealing with the intermittent nature of renewable energy sources.[5,6] Till date, major progress has been limited to two-electron products of the CO_2RR due to the relatively easier two-electron-transferred electrocatalysis process and the generation of multielectron-transferred products with higher value remains a grand challenge.[7–10] Especially attractive is the tunable and selective production of multielectron=-transferred products, which is generally hard to achieve when taking the hardness of CO_2 adsorption/activation, the multiproton/electron transfer process, and rational design of product-selective electrocatalysts into consideration. In addition, the competitive hydrogen evolution reaction (HER) further affects the final products and results in low selectivity.[11,12] Therefore, it is both scientifically and practically appealing to explore powerful electrocatalysts for the tunable and selective production of multielectron-transferred products with high efficiency.

Cu has been surveyed as the only active metal for electrochemically catalyzing CO_2 into multielectron-transferred products on account of its negative adsorption energy for CO* and positive adsorption energy for H* compared with other transition-metal systems.[13,14] Various electroreduction products such as CO, HCOOH, CH_4, C_2H_4, and C_2H_5OH have been reported for Cu-based electrocatalysts.[15–17] Notwithstanding, different kinds of electrocatalysts or complex techniques are needed to produce varied and selective products in electrochemical CO_2RR, which increase not only the cost but also the energy consumption.[18] Therefore, it is worth paying much attention to design similar types of catalysts that can produce drastically changed and

valuable products with high selectivity to meet the unmet demand of varied feedstock in the CO_2RR, where these systems could minimize the cost or energy consumption in production. Under this guidance, some pioneering works reported that crystal facet engineering or morphology control can adjust the selectivity of electroreduction products in Cu-based electrocatalysts.[19,20] For example, studies on Cu_2O nanoparticles showed that the selectivity and activity of C_2H_4 production depend strongly on the different crystal facets exposed.[20] However, there are also drawbacks for the state-of-the-art catalysts, such as 1) the target products being mostly limited to one kind of product with low tunability or selectivity and few works discussing the control of C—C coupling steps for hydrocarbon production, where it remains a grand difficulty to circumvent; 2) most of the reported electroreduction electrocatalysts being nonporous and lacking a well-tuned morphology that might limit the CO_2 adsorption/activation or mass transfer process; and 3) the synthesis methods for electrocatalysts generally being hard to scale up for production.

In addition, prior studies on morphology control show that hollow catalysts with the nanocavity confinement structure can suppress the loss of carbon intermediates and increase the chance for C—C coupling.[21,22] In view of this, powerful electrocatalysts with well-tuned morphology such as hollow structures that are beneficial for mass transfer and having potential in tuning the production of varied electroreduction products with high selectivity are desirable.[23,24] In general, it is hard to generate the hollow sphere morphology for most materials due to the lack of intensive self-assembly during the formation process. Specifically, metal–organic polyhedra (MOP) or modified MOP that are mostly soluble and stable in proper solvents might serve as desired candidates for self-assembly with additives such as polymers to generate hollow structures.[25] Therefore, we propose the strategy of self-assembly of hydroxyl Cu-MOP and a polymer into Cu-based hollow spheres for selective CO_2 electroreduction. We intend to select MOP-2 (a kind of hydroxyl-functionalized Cu-MOP) and a triblock polymer (i.e., F127) to investigate the

possible interaction between them and the hydroxyl groups might self-assemble with the hydrophilic portions of F127 to achieve hollow sphere morphology, whereas the nonmodified Cu-MOP would result in irregular morphology due to the lack of strong interaction (**Figure 1**). To the best of our knowledge, the self-assembly of hydroxyl Cu-MOP and a polymer into Cu-based hollow spheres as CO_2 electrocatalysts for tunable and selective production of multielectron-transferred products has been rarely reported.

Herein, we have prepared a series of Cu-based hollow spheres (PISG-x, $x = 1$–9, x stands for the mass ratio of F127 and MOP-2 in the precursors) through a polymer-induced sol–gel (PISG) method. The morphology of the catalysts can be easily tuned with different ratios of F127 and MOP-2,[25,26] resulting in different compositions with precisely controlled hollow sphere morphology. Specifically, one of them, PISG-3, shows a maximum of 61.1% (-0.9 V, -143 mA cm^{-2}) Faradaic efficiency (FE) of C_2H_4 and negligible CH_4, which is higher than that of PISG-1 ($FE_{C_2H_4}$ 46.7%, -0.9 V) with solid-sphere morphology. Interestingly, $CaCO_3$ has been proven to accurately adjust the inherent property of Cu-based hollow spheres, thus leading to the fine-tuning of the production of varied electroreduction products from C_2H_4 to CH_4 with largely increased hydrocarbon selectivity and CO_2 reduction efficiency. Notably, PISG-8 with slightly modified composition shows drastically changed products (FE_{CH_4} 55.8% and $FE_{C_2H_4}$ 22.2%, -162 mA cm^{-2}, -0.9 V) and a higher selectivity for hydrocarbons (78.0%) under similar conditions. Based on the DFT calculations, the addition of $CaCO_3$ has proven to play the role that it can decrease the possibility for coexistence of two adjacent *CHO to restrain the dimerization process and enhance the activity and selectivity. We report the first case of $CaCO_3$-decorated Cu-based hollow spheres that can not only adjust the selectivity of products but also improve the CO_2 reduction efficiency. In addition, the method is easy to scale up for production and the ≈ 0.5 g sample can be readily synthesized in a batch experiment.
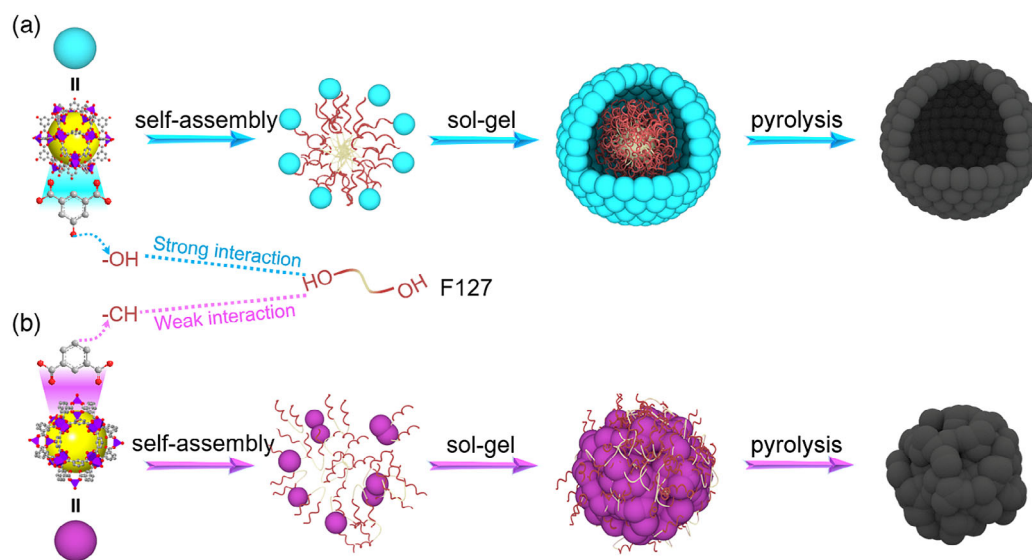

Figure 1. Schematic representation of the preparation of samples from the self-assembly of hydroxyl Cu-MOP or Cu-MOP with F127. a) Hollow spheres from the self-assembly of hydroxyl Cu-MOP and F127. b) Solid nanoparticles from the self-assembly of Cu-MOP and F127.

**ADVANCED
SCIENCE NEWS**
www.advancedsciencenews.com

**small
structures**
www.small-structures.com

2. Results and Discussion

The PISG method is listed as follows. First, a certain amount of Ca-decorated triblock copolymer F127 ($EO_{106}PO_{70}EO_{106}$, Ca: 0.47 wt%) is dissolved in ethanol to form a kind of homogeneous solution. Then, hydroxyl-functionalized MOP-2 is added, followed by stirring for half an hour. After that, a kind of blue hydrogel is generated after staying static at room temperature for 24 h. After ethanol evaporation, a kind of dry hydrogel is achieved. A black powder is obtained after heat treating at 400 °C for 5 h. Through tuning the mass ratio of Ca-decorated F127 and MOP-2, a series of products named PISG-x ($x = 1$–9; for details see Experimental Section) is obtained. In addition, MOP-1 (isoreticular to MOP-2 without hydroxyl groups) is applied to replace MOP-2 to synthesize contrast samples for further characterization (Figure S1–S3, Supporting Information).[27] Taking PISG-8, for example, powder X-ray diffraction (PXRD) tests indicate the existence of mixed components for CuO (JCPDS No. 80-1268) and $CaCO_3$ (JCPDS No. 47-1743)

(**Figure 2**a). Similarly, all the other PISG-x samples show similar components in the PXRD tests (Figure S4, Supporting Information). To further verify the result, Fourier-transform infrared spectroscopy (FT-IR) tests were conducted and the peak at 530 cm^{-1} was assigned to the stretching vibration of Cu—O, indicating the main composition of CuO (Figure S5, Supporting Information). The result was further supported by Raman tests and the peaks at 284, 345, and 620 cm^{-1} are attributed to CuO (Figure S6, Supporting Information).[28] To evaluate the porosity of the materials, N_2 sorption tests were conducted, and the samples show high porosity (Figure S7, Supporting Information). For example, PISG-8 exhibits a Brunauer–Emmett–Teller surface area (S_{BET}) of 84 $m^2 g^{-1}$ with a pore volume (V_t) of 0.18 $cm^3 g^{-1}$, almost triple that of carbonized MOP-2 (C-MOP-2) (S_{BET} 30 $m^2 g^{-1}$ and V_t 0.06 $cm^3 g^{-1}$) (Figure S7a and Table S1, Supporting Information). Moreover, the pore size distribution shows the pore of the sample distributes from ≈2 to ≈24 nm, implying the existence of mesopores in PISG-8 (Figure S7b, Supporting Information). In contrast, the
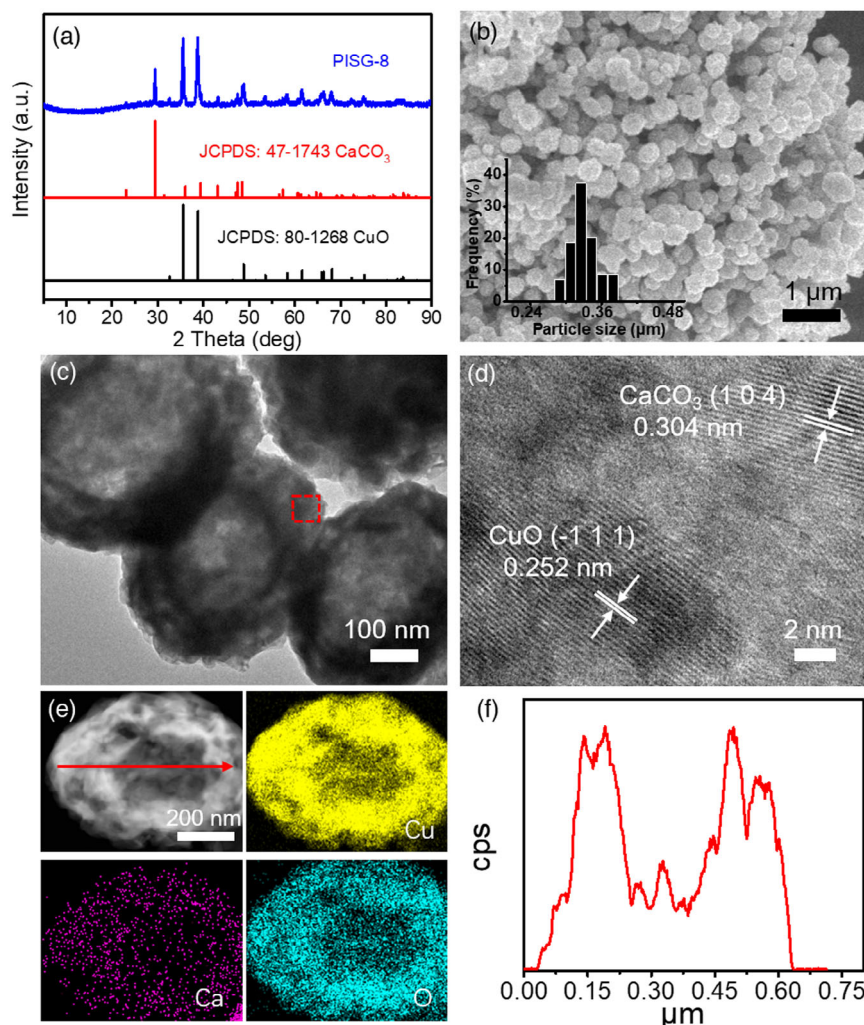

Figure 2. Structure and characterization of PISG-8. a) PXRD patterns of PISG-8. b) Scanning electron microscopy (SEM) image. c) Transmission electron microscopy (TEM) image. d) High-resolution transmission electron microscopy (HR-TEM) image. e) Scanning transmission electron microscopy (STEM) and elemental mapping images. f) Linear scan image of Cu.

carbonized F127 (C-F127) shows an S_{BET} of 140 m^2 g^{-1} with a V_t of 0.24 cm^3 g^{-1} (Table S1, Supporting Information). Therefore, the higher S_{BET} for PISG-8 than that of C-MOP-2 might be ascribed to the addition of the template F127.

To explore the electronic state of PISG-8, X-ray photoelectron spectroscopy (XPS) was conducted.[29] The high-resolution XPS spectrum of Cu 2p shows only one valence state and the binding energies at 933.5 and 953.7 eV are ascribed to Cu^{2+} 2$p_{3/2}$ and 2$p_{1/2}$, respectively (Figure S8a, Supporting Information).[30–32] The Ca 2p spectrum shows two peaks at 350.1 and 346.3 eV, revealing the presence of CaCO$_3$ (Figure S8b, Supporting Information).[33] Furthermore, the C 1s spectrum displays two peaks at 284.6 eV (C—C) and 289 eV (O—C=O) (Figure S8c, Supporting Information).[34] The O 1s spectrum can be deconvoluted into a strong peak of C=O at 530.8 eV and a relatively weak peak of Cu—O at 529.3 eV (Figure S8d, Supporting Information).[35] Similarly, XPS tests of PISG-3 and C-MOP-2 were further conducted to study their relative electronic states (Figure S9 and S10, Supporting Information). The mass ratios of Cu/Ca and C and O contents of the obtained samples (PISG-x) were evaluated based on inductively coupled plasma optical emission spectrometry (ICP-OES) and elemental analysis (Table S2, Supporting Information). For example, PISG-3, PISG-5, and PISG-8 show Cu/Ca mass ratios of 5.61, 4.12, and 2.71, respectively (Table S2, Supporting Information).

To further characterize the morphology of the samples, scanning SEM and TEM tests were performed. Taking PISG-8, for example, a kind of uniform sphere morphology with a diameter of ≈340 nm was detected in the SEM image (Figure 2b). The thickness of the hollow sphere was calculated to be ≈100 nm in the TEM image (Figure 2c). In the HR-TEM test, the lattice spacing of 0.252 nm is ascribed to (−111) crystalline planes of CuO (Figure 2d). The lattice spacing of 0.304 nm is attributed to (104) crystalline planes of CaCO$_3$, indicating the coexistence of CuO and CaCO$_3$. The hollow-sphere morphology was further certified by the linear scanning of energy dispersive X-ray spectrometry (EDS), in which a volcano-type distribution curve can be detected for the Cu element (Figure 2f and Figure S11, Supporting Information). A similar phenomenon has been observed for Ca and O elements in the linear scanning of EDS tests (Figure S12, Supporting Information). Moreover, high-angle annular dark-field scanning transmission electron microscopy (HAADF-STEM) and the corresponding element mapping images of PISG-8 show that Cu, Ca, and O are uniformly distributed in the hollow sphere (Figure 2e). PISG-3, with a slightly changed composition, displays a similar hollow-sphere morphology (diameter ≈460 nm and thickness ≈80 nm) with uniformly distributed elements as revealed by various morphology characterizations (Figure S13, Supporting Information). For other samples, PISG-1 with the highest MOP-2 percentage in the precursor shows a solid-sphere morpholgoy (Figure S14a,b, Supporting Information). With increasing percentage of F-127, PISG-2 to PISG-9 all display a hollow-sphere morphology with approximate diameter 280–620 nm and thickness 70–100 nm) (Figure S14 and S15, Supporting Information). These results suggest that PISG-x is a kind of CaCO$_3$-decorated Cu-based hollow sphere with tunable composition.

To explore the formation process of the hollow-sphere morphology, we set out to explore the possible formation mechanism with the support of various contrast samples. During the self-assembly process, the triblock copolymer F127 containing hydrophilic and hydrophobic portions might be self-assembled with the hydrophilic portion (i.e., hydroxyl groups) of MOP-2 to generate the hydrogel in the solvent (Figure 1a). Then, the self-assembled material is transferred into the hollow-sphere morphology during the pyrolysis process. We speculate that there are some vital factors in the formation of the hollow-sphere structures: 1) the solubility and the hydroxyl groups of MOP-2, which can serve as homogeneous media to fully interact with the hydrophilic groups in F127; 2) the hydrophilic parts of F127, which can assemble with hydroxyl groups in MOP-2, while leaving the hydrophobic portions to connect together to generate the sphere morphology; and 3) the formation of a sol–gel system, which is probably beneficial for the shaping of the hollow-sphere morphology during the pyrolysis process, etc. Based on these, we take a series of contrast experiments to support the superiority of the PISG method in the generation of the hollow-sphere morphology. Contrast samples such as C-MOP-2 and C-F127 display a solid morphology with a nonuniform and nonporous morphology as revealed by the SEM and TEM tests (Figure S16 and S17, Supporting Information). In addition, the contrast sample that replaces MOP-2 with MOP-1 shows a nonuniform and nonporous morphology, which may be because MOP-1 without a hydroxyl group cannot provide sufficient interaction with F127 (Figure 1b and S18, Supporting Information). Then, CuCl$_2$, a soluble copper salt, was selected to replace MOP-2 in the PISG method, while the carbonized morphology was still nonuniform and nonporous (Figure S19, Supporting Information). In addition, to further support the importance of F127 in the formation process, polyvinylpyrrolidone K30 (PVP) was applied to replace F127 during the preparation process. The result shows that PVP cannot produce a hydrogel with MOP-2 and the carbonized morphology is irregular (Figure S20, Supporting Information). Above all, the PISG-x method is based on the self-assembly of specially selected MOP-2 and F127 that can precisely control the generation of a hollow-sphere morphology.

The specially designed Cu-based hollow spheres with tunable composition might serve as desirable platforms to investigate the generation of different products in the electrochemical CO$_2$RR. To test their performance, PISG-x was packaged in flow cells and tested in a three-electrode electrochemical system with 1 M KOH solution as the electrolyte. The reason for applying an alkaline electrolyte (1 M KOH) during the electrochemical CO$_2$RR process is that the high pH would be favorable for suppressing the HER and enhancing the CO$_2$RR properties.[16] In this work, all the potentials are measured using a Ag/AgCl electrode and the results are reported relative to the reversible hydrogen electrode (RHE).

Taking PISG-3 and PISG-8 as two examples, the LSV curves reveal that PISG-3 and PISG-8 enable electrochemical CO$_2$RR at a potential less than −0.4 V (**Figure 3**a). PISG-3 and PISG-8 have a much higher current density in the electrochemical CO$_2$RR than in the HER at a wide potential range (−0.4 to −1.2 V vs RHE), suggesting that PISG-3 and PISG-8 favor the electrochemical CO$_2$RR over the HER (Figure 3a). The electrochemical CO$_2$RR polarization curves of PISG-3 and PISG-8 abruptly take off at ≈−0.45 V, increase sharply, and reach −240 and −270 mA cm^{-2} at −1.1 V, respectively (Figure 3b). To support the superiority of the sample with the hollow-structure
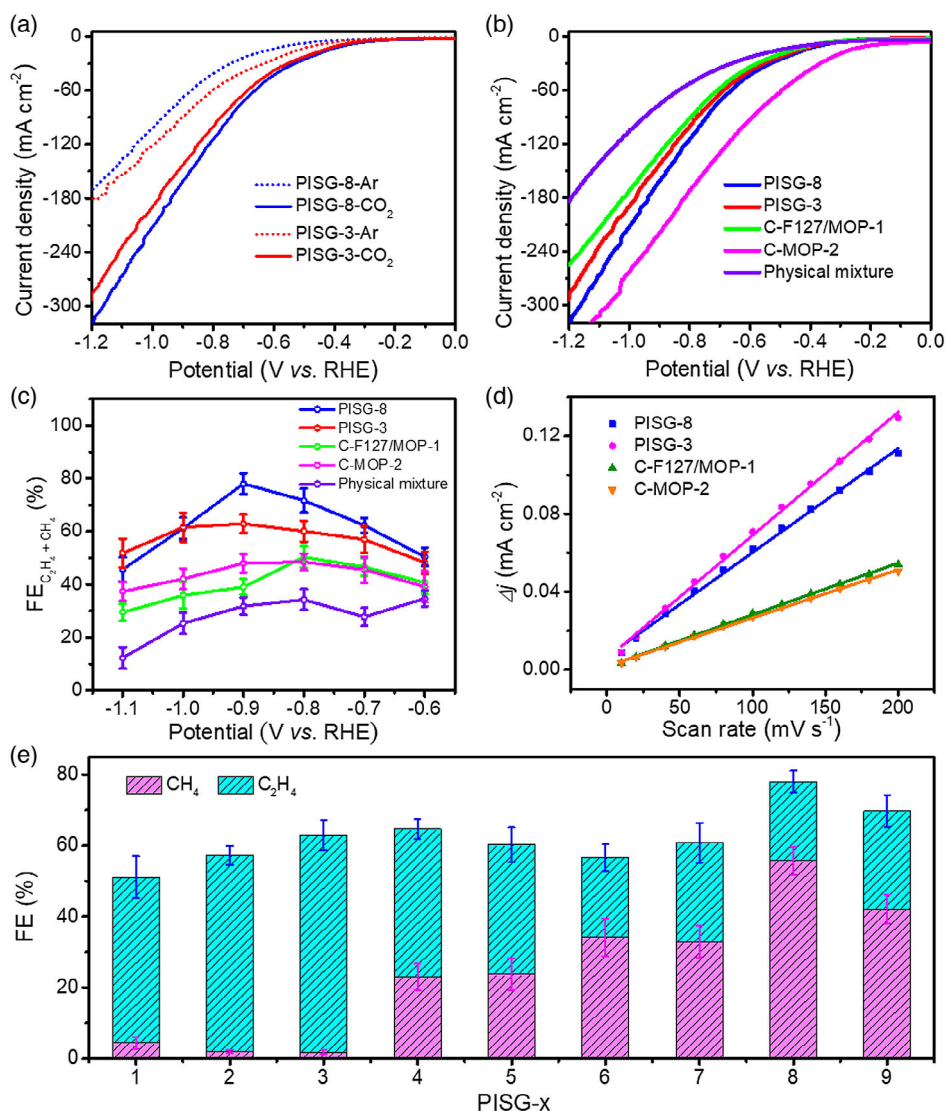
Figure 3. Electrocatalytic performance of PISG-8, PISG-3, C-F127/MOP-1, C-MOP-2, and physical mixture of C-F127 and C-MOP-2. a) Linear sweep voltammetric (LSV) curves of PISG-8 and PISG-3 in Ar and CO_2 atmosphere. b) LSV curves of PISG-8, PISG-3, C-F127/MOP-1, C-MOP-2, and physical mixture. c) Faradaic efficiency ($CH_4 + C_2H_4$) of PISG-8, PISG-3, C-F127/MOP-1, C-MOP-2, and the physical mixture at different applied potentials (−0.6 V to −1.1 V). d) The corresponding capacitive current at 0 V versus Ag/AgCl as a function of scan rate (10–200 mV s^{-1}) for PISG-8, PISG-3, C-F127/MOP-1, and C-MOP-2. e) Faradaic efficiency for CH_4 and C_2H_4 of PISG-x (PISG-1–PISG-9) at −0.9 V versus RHE. All the reported values are average ones calculated from three or more independent measurements, and all the errors are given as standard deviations.

morphology, we also tested the properties of C-F127, C-MOP-2, C-F127/MOP-1, and the physical mixture of C-F127 and C-MOP-2. The current density of PISG-8 (−162 mA cm^{-2}) is higher than that of PISG-3 (−143 mA cm^{-2}), C-F127/MOP-1 (−130 mA cm^{-2}), and the physical mixture (−76 mA cm^{-2}) at the potential of −0.9 V (Figure 3b). Furthermore, to evaluate the selectivity of catalysts, electrocatalysis reactions were conducted at different potentials and the reduction products were detected by gas chromatography (GC). For PISG-3, C_2H_4 is the main product and an $FE_{C_2H_4}$ of 46.1% with a partial current density of −17.7 mA cm^{-2} has been detected at −0.6 V. With the increase of potential, the $FE_{C_2H_4}$ continuously enhances and a maximum $FE_{C_2H_4}$ of 61.1% with negligible CH_4 (1.8%) is achieved at the

potential of −0.9 V (Figure S21b, Supporting Information). In contrast, CH_4 is the main product for PISG-8 (FE_{CH_4} 42.5%; $FE_{C_2H_4}$ 19.8%) with a partial current density of −31 mA cm^{-2} at the potential of −0.7 V. With the increase of potential, the FE_{CH_4} enhances and PISG-8 has a maximum value of 55.8% at −0.9 V, whereas the $FE_{C_2H_4}$ changes only slightly to 22.2% (Figure 3c and S21a, Supporting Information). Furthermore, C-F127 exhibits poorer performance with FE_{H_2} higher than 90% at each potential (−0.7 to −1.0 V) (Figure S22a, Supporting Information). C-MOP-2 only shows a $FE_{CH_4+C_2H_4}$ of 48% at −0.9 V (Figure 3c). In addition, C-F127/MOP-1 and the physical mixture sample exhibit $FE_{CH_4+C_2H_4}$ values of ≈40% and ≈30% at −0.9 V, respectively, in accordance with the nonuniform and

nonporous morphology as mentioned earlier (Figure S22 and S23, Supporting Information). Furthermore, the partial current densities of CH_4, C_2H_4, and H_2 were calculated to reveal the superior activity of PISG-3 and PISG-8 over contrast samples (Figure S24, Supporting Information). These results reveal that samples with hollow-sphere morphology exhibit much better performance than contrast samples, suggesting the superiority of hollow spheres, which might expose more active sites and are beneficial for the mass transfer to improve the electrocatalytic properties.

Moreover, to estimate the electrochemical active surface area (ECSA) and discuss the potential influence factors, the electrochemical double-layer capacitance (C_{dl}) was calculated and analyzed (Figure 3d). The obtained results show that samples such as PISG-3 (0.63 mF cm^{-2}) and PISG-8 (0.53 mF cm^{-2}) present $\approx$2 times increased C_{dl} values than contrast samples such as C-F127/MOP-1 (0.27 mF cm^{-2}) and C-MOP-2 (0.25 mF cm^{-2}) under similar conditions (Figure S25, Supporting Information). The results indicate that the hollow-sphere structure might provide tremendous active sites that are beneficial for efficient mass transfer. In addition, the charge transfer resistance of PISG-8, PISG-3, C-F127/MOP-1, and C-MOP-2 were calculated to be 0.14, 0.16, 0.17, and 3.50 Ω, respectively. The results further confirm the lower charge transfer resistance and faster electron transfer efficiency for PISG-3 and PISG-8 (Figure S26, Supporting Information).

Furthermore, the effect of different precursors on the electrocatalyst properties was investigated and distinct performances have been detected in electrochemical CO_2RR. Interestingly, PISG-1–PISG-3 overall show the trend of gradually increasing $FE_{C_2H_4}$, and PISG-4–PISG-9 display an enhanced trend of FE_{CH_4} (Figure 3e). Upon tuning the mass ratio of F127 and MOP-2 in the initial precursors from PISG-1 to PISG-3, the products are mainly C_2H_4 at −0.9 V with negligible CH_4 (i.e., $FE_{C_2H_4}$ PISG-1 46.7%; PISG-2 55.3%; and PISG-3 61.1%) (Figure S27, Supporting Information). For example, C_2H_4 is the major product for PISG-3 and the $FE_{C_2H_4}$ can reach up to a maximum value of 61.1% at the potential of −0.9 V with negligible CH_4 (Figure S21b, Supporting Information). Interestingly, CH_4 starts to be detected for PISG-4, which results in a mixed product of CH_4 (FE_{CH_4} 23.0%, −0.9 V) and C_2H_4 ($FE_{C_2H_4}$ 41.7%, −0.9 V). For samples PISG-4–PISG-9, the FE_{CH_4} gradually increases with the decrease of C_2H_4 (i.e., FE_{CH_4} PISG-5 23.7%; PISG-6 34.2%; PISG-7 33.0%; and PISG-8 55.8%; $FE_{C_2H_4}$ PISG-5 36.5%; PISG-6 22.4%; PISG-7 27.9%; and PISG-8 22.2%) (Figure S28, Supporting Information). It is noteworthy that the total $FE_{CH_4+C_2H_4}$ (78.0%) of PISG-8 is superior to that of most of the reported Cu-based electrocatalysts (**Figure 4**c and Table S3, Supporting Information).[4,13] However, the increase trend stops for PISG-9 (FE_{CH_4} 42.1%; $FE_{C_2H_4}$ 27.6%, −0.9 V), possibly attributed to the much lower amount of active sites as for the excessive addition of F127 (Figure S28, Supporting Information).

Based on the aforementioned interesting phenomenon that electrocatalytic properties can be drastically changed with the tuning of precursors, we embark on the investigation of the possible mechanism, which is also vital in the rational design of suitable electrocatalysts for the selective generation of target products. Based on various characterizations, the drastic change of the products might be closely related to the varied compositions

of PISG-x. Commercial $CaCO_3$ can only produce H_2 under electrochemical CO_2RR conditions (Figure S29, Supporting Information). As mentioned earlier, C-F127 shows FE_{H_2} higher than 90% at each potential (−0.7 to −1.0 V) (Figure S22a, Supporting Information) and C-MOP-2 shows a 40% $FE_{C_2H_4}$ (−0.9 V) with negligible CH_4 (Figure S22b, Supporting Information). We suppose that the addition of $CaCO_3$ is responsible for the drastic change of products. To further reveal the effect of $CaCO_3$ on the generation of different reduction products, S-F127 (stands for F127 purchased from Sigma, without the addition of Ca) was selected as the precursor to prepare various contrast samples (S-PISG-x, x = 3–8) without $CaCO_3$ as proved by the PXRD tests (Figure S30, Supporting Information). The FE tests show that the main products of S-PISG-3 to S-PISG-8 are C_2H_4, with negligible CH_4, indicating that the production of CH_4 originates from the effect of $CaCO_3$ (Figure S31, Supporting Information). We have also introduced $CaCO_3$ in S-PISG-8 by adding calcium chloride to the precursor to validate the effect of $CaCO_3$, the obtained main product of CH_4, which possesses a similar result to PISG-8 (Figure S32, Supporting Information). In addition, in PISG-x (x = 1–9), samples with higher $CaCO_3$ contents offer a greater tendency to generate more CH_4 during the electrochemical CO_2RR process, while electrocatalysts with lower ones are more likely to generate more C_2H_4, possibly due to the doping of $CaCO_3$, which can adjust the C—C coupling process during the electrochemical CO_2RR process.

An isotopic experiment using $^{13}CO_2$ as substrate was performed under identical reaction conditions to reveal the carbon source of electrochemical CO_2RR products. The peak at $m/z = 17$ and $m/z = 30$ are assigned to $^{13}CH_4$ and $^{13}C_2H_4$, respectively, indicating that the carbon sources of CH_4 and C_2H_4 indeed derive from the CO_2 used (Figure 4a,b). In addition, PXRD test analyses of the products after electrochemical tests were conducted. PISG-8 demonstrates remained phases of CuO (JCPDS No. 80-1268) and $CaCO_3$ (JCPDS No. 47-1743) as the sample before electrochemical CO_2RR (Figure S33, Supporting Information). To characterize the morphology of the electrocatalysts after electrocatalysis, SEM and TEM tests were performed. Taking PISG-3 as an example, a kind of uniform sphere morphology with a diameter of $\approx$350 nm is detected in the SEM and TEM images, which matches well with the pristine state before the test (Figure S34a,b, Supporting Information). To reveal the inner crystal phase of electrocatalysts, the HR-TEM tests were conducted. Crystalline planes of (−111) and (104) that are ascribed to CuO and $CaCO_3$, respectively, (Figure S34c, Supporting Information) could be detected, which are in accordance with the results before the test (Figure S13d, Supporting Information). The HAADF-STEM and corresponding element mapping images of PISG-3 after CO_2RR test show that Cu, Ca, and O are uniformly distributed in the hollow sphere (Figure S34d, Supporting Information). Furthermore, obvious lattice stripes that correspond well with the crystal face (111) of Cu (JCPDS No. 1-1241) are visible (Figure S35, Supporting Information).[36–38] EDS tests displayed the existence of Ca in both PISG-3 and PISG-8 after CO_2RR electrocatalysis (Figure S36, Supporting Information). In addition, the compositions of the electrocatalytic samples analyzed by XPS tests show the presence of Cu^{2+} and Cu^0 (Figure S37, Supporting Information).[32,39]
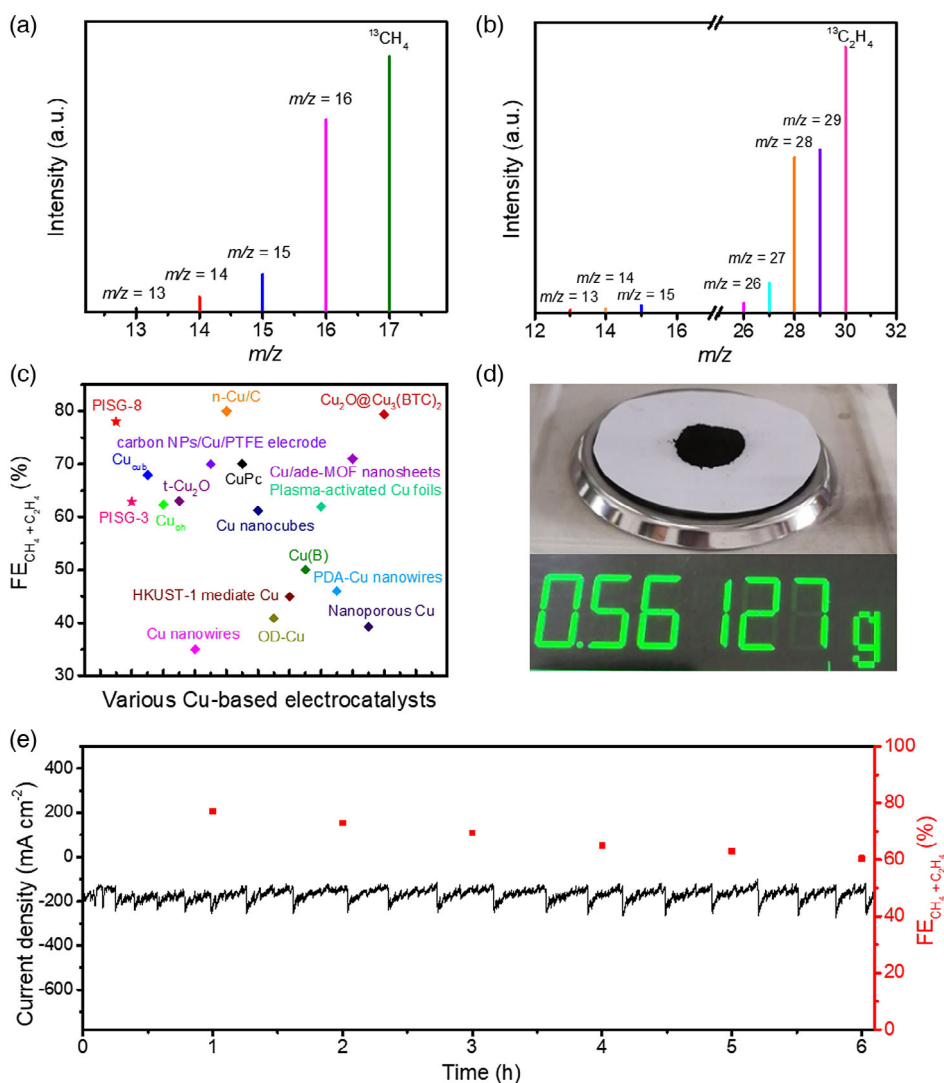
Figure 4. Characterization of PISG-x. a) The mass spectra of $^{13}CH_4$ recorded under a $^{13}CO_2$ atmosphere for PISG-8. b) The mass spectra of $^{13}C_2H_4$ recorded under a $^{13}CO_2$ atmosphere for PISG-8. c) The $FE_{CH_4+C_2H_4}$ of some representative Cu-based electrocatalysts. d) A photo of the scale-up sample (the photo shown is reconnected to clearly give the mass data). e) Durability test of PISG-8 at the potential of -0.9 V versus RHE.

Stability is a key factor to evaluate the durability properties of electrocatalysts.[40–42] To analyze the electrochemical stability of PISG-8, durability tests were conducted at the potential of -0.9 V for 6 h (Figure 4e and Figure S38, Supporting Information). During the process, the corresponding $FE_{CH4+C2H4}$ can be maintained at values of more than 60% and the current density is ≈ -180 mA cm^{-2} over the entire experiment. These results demonstrate that PISG-8 is a kind of stable electrocatalyst, which has much potential to be used in efficient electrochemical CO_2RR. In addition, the samples are ease in large-scale production and ≈ 0.5 g sample of PISG-8 can be readily produced in a batch experiment on a lab scale (Figure 4d), holding much promise in the development of a facile and scalable method in the production of a product-selective electrochemical CO_2RR system.

To understand the high activity as well as the selective production reaction mechanism of PISG-x, DFT calculations were implemented (**Figure 5**). First, principle-based analysis was

implemented to gain an atomic-scale understanding of the role of $CaCO_3$. Considering the pristine state of CuO in PISG-x, which might be transferred into mixed components of CuO, Cu^0, or Cu^+ species with changeable composition, crystallinity, or interface interaction during the electrocatalysis process, it is quite difficult to accurately construct a desired model to simulate most CuO-based electrocatalysts with current techniques.[36,39] After making tremendous endeavors, we propose a possible strategy that combines CuO with $CaCO_3$ (the original component of the electrocatalyst) to construct a hybrid material model (i.e., CuO–$CaCO_3$) according to the experimental results. The computational hydrogen electrode method proposed by Norskov et al.[43–45] is introduced and demonstrated in detail in the Supporting Information, by which we can study the CO_2RR process (Figure S39–41, Supporting Information). This model can partially simulate the possible interaction between CuO and $CaCO_3$ and serve as a platform to investigate the possible
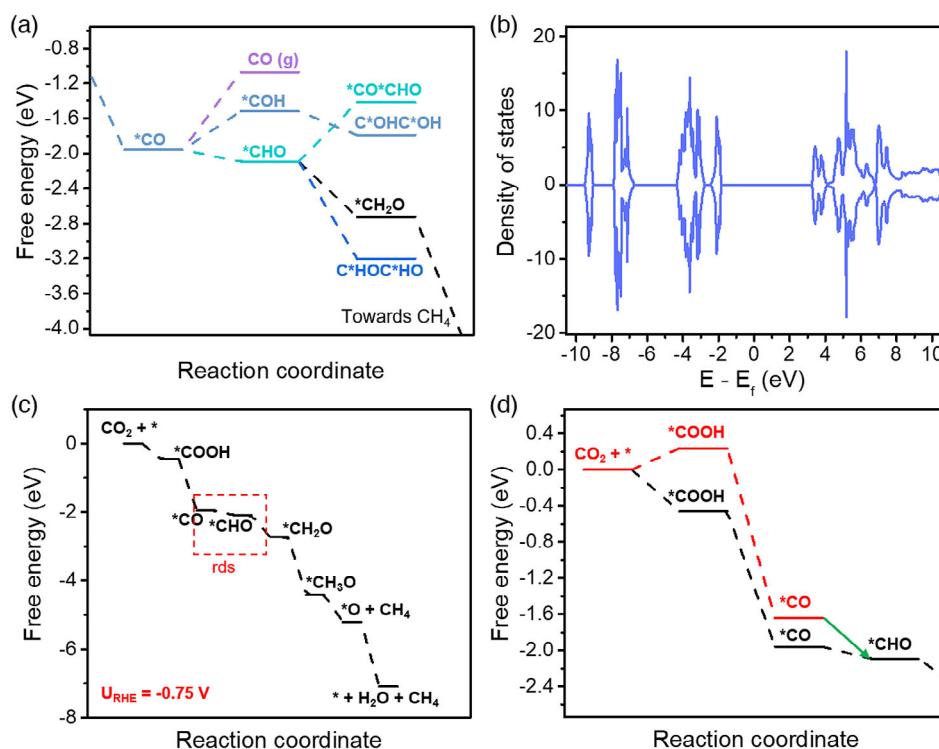
**ADVANCED
SCIENCE NEWS**
www.advancedsciencenews.com

**small
structures**
www.small-structures.com

Figure 5. DFT calculations for the role of $CaCO_3$ in the electrochemical CO_2RR. a) The FED of the dimerization process, where U_{RHE} is set at -0.75 V. b) Calculated density of states (DOS) of $CaCO_3$. c) FED of the CH_4 pathway on CuO. d) The red and black stepwise plots are the calculated FEDs of the CO_2RR on Cu sites at $CuO–CaCO_3$ and CuO, respectively, where the latter is directly copied from (c). In (d), the green arrow shows an extra route that is created for $CuO–CaCO_3$.

function of $CaCO_3$. Figure 5a shows the reaction free-energy diagram (FED) of the dimerization-associated steps, where the exact dimerization process in CuO is preferred to $*CHO + *CHO \rightarrow C*HOC*HO$ over other steps. Moreover, the CH_4 process is less favorable than dimerization on CuO as indicated by the higher energy level of $*CH_2O$ than $C*HOC*HO$ (Figure 5a), whereas the reaction scheme changes when $CaCO_3$ is brought in. $CaCO_3$ is an insulator, as revealed by the calculated DOS plot (Figure 5b). Furthermore, the key intermediate $*CO$ cannot be chemically adsorbed on $CaCO_3$ during the structure optimization. These results indicate that $CaCO_3$ alone is inert for the CO_2RR. Therefore, considering the dimerization process requests the coexistence of two adjacent $*CHO$, when inert $CaCO_3$ occupies a big portion of the surface sites, the possibility for dimerization largely decreases. The C_2 pathway is then restrained, which turns the C_1 pathway to the favorable pathway for the CO_2RR. The calculated results are consistent with the experiments, as mentioned earlier (Figure 3e). Moreover, the existence of $CaCO_3$ can also improve the activity of the CO_2RR. As indicated by the red stepwise plot in Figure 5d, the $*CO$ adsorption on $CuO–CaCO_3$ is slightly weaker than on CuO, suggesting the existence of $CaCO_3$ will bring in an additional faster reaction route. This is marked by a green arrow in Figure 5d, where evidently the thermodynamic barrier for $*CO + H^+ + e \rightarrow *CHO$ is lessened than in the black stepwise scheme. As $*CO + H^+ + e \rightarrow *CHO$ is the rate-limiting step of the CO_2RR, the activity for the CO_2RR is then increased.

Above all, the addition of $CaCO_3$ can decrease the possibility for coexistence of two adjacent $*CHO$ to restrain the dimerization process and improve the selectivity and activity for the CH_4 product, as revealed by the outstanding FE_{CH4} for samples with relatively high loading of $CaCO_3$, such as PISG-8, whereas samples with lower loading of $CaCO_3$, such as PISG-3, have a greater tendency for production of C_2H_4. Tuning the loading amount of $CaCO_3$ in PISG-x enables selective production of varied products in the CO_2RR as certified by the results as discussed earlier. Despite the inspiring results obtained from the DFT calculations that can prove the unique function of $CaCO_3$ to some extent, still more efforts are needed for designing perfect simulation models to actually reflect the electrocalysis environments, such as the composition, morphology, crystallinity, interface interaction, and valence states.

3. Conclusion

In summary, we have successfully synthesized a series of Cu-based hollow spheres through the self-assembly of hydroxyl MOP and F127 with a polymer induced sol–gel method. The specially designed Cu-based hollow spheres with well-tuned morphology and composition endow the materials with an adjustable inherent property, thus leading to the fine-tuned production of varied electroreduction products with high selectivity in the electrochemical CO_2RR. Specifically, PISG-3 presents a

**ADVANCED
SCIENCE NEWS**
www.advancedsciencenews.com

**small
structures**
www.small-structures.com

maximum $FE_{C_2H_4}$ of 61.1% (−0.9 V, −143 mA cm^{-2}) and negligible CH_4, which is higher than that of PISG-1 ($FE_{C_2H_4}$ 46.7%, −0.9 V) with solid-sphere morphology. Interestingly, $CaCO_3$ has been proven to modify the inherent property of Cu-based hollow spheres and it has the ability to fine-tune the production of varied electroreduction products from C_2H_4 to CH_4 with largely increased hydrocarbon selectivity and CO_2 reduction efficiency. Notably, PISG-8 with a slightly modified composition shows drastically changed products (FE_{CH_4} 55.8% and $FE_{C_2H_4}$ 22.2%, −162 mA cm^{-2}, −0.9 V) and a higher selectivity for hydrocarbons (78.0%) under similar conditions. Based on the DFT calculations, the addition of $CaCO_3$ has been proven to play the roles that it can decrease the possibility for coexistence of two adjacent *CHO to restrain the dimerization process and enhance the activity. In this work, we report the first case of $CaCO_3$-decorated Cu-based electrocatalysts that can not only adjust the selectivity of products but also improve the CO_2 reduction efficiency. In addition, the ≈0.5 g sample can be readily and facilely synthesized in a batch experiment. This work provides a novel and feasible pathway to design Cu-based hollow-sphere electrocatalysts for product-selective electrochemical CO_2RR, holding much promise in powerful industrial processes such as multistep or fluid-bed catalysis systems.

4. Experimental Section

Synthesis of MOP-2 and Preparation of PISG-x: The synthesis of MOP-2 followed a previsouly reported method with slight modification.[25] In detail, 0.36 g 5-hydroxy-1,3-benzenedicarboxylic acid was dissolved in 10 mL methanol solution in a 50 mL glass vial under stirring. $Cu(OAc)_2 \cdot H_2O$ (0.40 g) was predissolved in 30 mL methanol and added to a glass vial, followed by stirring for 30 min at room temperature. After that, 10 mL *N,N*-dimethylacetamide (DMA) was added to the solution and the glass vial was transferred to the oven and heated at 85 °C for 24 h. After cooling to room temperature, the product was washed with DMA and dichloromethane three times. After drying at 60 °C for 24 h under vacuum, a blue powder was obtained.

The PISG method to prepare PISG-x (x stands for the mass ratio of F127 and MOP-2 in the precursors; the mass ratios of PISG-1–PISG-9 are 1:1, 3:1, 5:1, 6:1, 7:1, 8:1, 9:1, 10:1, and 11:1, respectively) is listed as follows. Taking PISG-8 as an example, 1.00 g Ca-decorated triblock copolymer F127 ($EO_{106}PO_{70}EO_{106}$, Ca: 0.47 wt%) was first dissolved in 40 mL ethanol under stirring to obtain a homogenous solution. Then 0.10 g MOP-2 was added into the solution, followed by stirring for half an hour. A kind of blue hydrogel was achieved after staying static at room temperature for 24 h. After ethanol evaporation (≈3 days), a kind of dry hydrogel was produced. The black powder was obtained after heat treating at 400 °C for 5 h (the heating rate was 5 °C min^{-1}) in a tubular furnace in the presence of an air atmosphere. In the synthesis of PISG-x, all of them were produced under similar procedures except that diverse amounts of MOP-2 were added (F127 remained the same and the amount of MOP-2 added followed the mass ratio of F127/MOP-2 for PISG-x).

The contrast samples of C-F127 and C-MOP-2 were directly treated with a similar heating process at 400 °C for 5 h (the heating rate was 5 °C min^{-1}) in a tubular furnace to that of PISG-8. For the synthesis of contrast samples such as C-PVP/MOP-2, C-F127/MOP-1, and C-F127/CuCl$_2$, all of the procedures followed similar steps to those for PISG-8 except F127 and MOP-2 were replaced with similar mass amounts of PVP, MOP-1, and CuCl$_2$, respectively. For C-F127/MOP-1, the part solubility of MOP-1 in ethanol led to slightly changed procedures. First, MOP-1 was produced from a hydrothermal method that followed a previously reported method,[27] in which isophthalic acid (0.42 mmol) and $Cu(NO_3)_2 \cdot 3H_2O$ (0.39 mmol) were mixed in DMF/ethanol (3:1, 10 mL) in a 20 mL glass vial, followed by heating at 85 °C for 24 h. The synthesis process of C-F127/MOP-1 was similar to that of PISG-8 except that MOP-1 was predissolved in dimethyl sulfoxide (DMSO) and mixed with F127 in ethanol solution. For the scale-up production of PISG-8, the synthesis process followed similar steps to those for PISG-8 except the amounts of precursors were expanded to 25 times. For the synthesis of contrast samples of S-PISG-x (x = 3–8), the procedure was similar to that for PISG-x (x = 3–8) expect that the Ca-decorated F127 was replaced by S-F127.

Material Characterization: PXRD tests of samples were recorded on a D/max 2500 VL/PC diffractometer (Japan) equipped with Cu Kα radiation (λ = 1.54060 Å) at 40 kV and 100 mA. FT-IR spectra were tested on a Bruker Tensor 27 FT-IR spectrophotometer. Raman spectra of powder samples were detected on a Lab-RAM HR800 with a laser excitation wavelength of 633 nm. Nitrogen adsorption–desorption isotherms were recorded at 77 K using a Quantachrome instrument (Quantachrome Instruments Autosorb IQ2). Before the measurement, the catalysts were degassed at 150 °C for 12 h. SEM and EDS of samples were analyzed by a scaning electron microscope (JEOL JSM-7600F) with an acceleration voltage of 10 and 15 kV, respectively. TEM, HRTEM, and STEM-HAADF images coupled to EDS elemental mapping were collected on a JEOL JEM-2100 electron microscope at 200 kV equipped with an Oxford Energy dispersive X-ray spectroscopy. ICP-OES (Leeman Labs) was applied to detect the contents of metal ions. The isotope-labeled experiment was performed using $^{13}CO_2$ instead of $^{12}CO_2$ and the result was analyzed by GC-MS (7890B and 5977B, Agilent). XPS tests were performed on a Thermo ESCALAB 250XI multifunctional imaging electron spectrometer using the binding energy of C as the internal standard.

Supporting Information

Supporting Information is available from the Wiley Online Library or from the author.

Conflict of Interest

The authors declare no conflict of interest.

Data Availability Statement

Research data are not shared.

[1] J. D. Shakun, P. U. Clark, F. He, S. A. Marcott, A. C. Mix, Z. Liu, B. Otto-Bliesner, A. Schmittner, E. Bard, *Nature* **2012**, *484*, 49.

[2] Y.-R. Wang, Q. Huang, C.-T. He, Y. Chen, J. Liu, F.-C. Shen, Y.-Q. Lan, *Nat. Commun.* **2018**, *9*, 4466.

[3] E.-X. Chen, M. Qiu, Y.-F. Zhang, Y.-S. Zhu, L.-Y. Liu, Y.-Y. Sun, X. Bu, J. Zhang, Q. Lin, *Adv. Mater.* **2018**, *30*, 1704388.

[4] C. Yang, S. Li, Z. Zhang, H. Wang, H. Liu, F. Jiao, Z. Guo, X. Zhang, W. Hu, *Small* **2020**, *16*, 2001847.

[5] O. S. Bushuyev, P. De Luna, C. T. Dinh, L. Tao, G. Saur, J. van de Lagemaat, S. O. Kelley, E. H. Sargent, *Joule* **2018**, *2*, 825.

[6] L. Fan, C. Xia, F. Yang, J. Wang, H. Wang, Y. Lu, *Sci. Adv.* **2020**, *6*, eaay3111.

[7] P.-P. Yang, X.-L. Zhang, F.-Y. Gao, Y.-R. Zheng, Z.-Z. Niu, X. Yu, R. Liu, Z.-Z. Wu, S. Qin, L.-P. Chi, Y. Duan, T. Ma, X.-S. Zheng, J.-F. Zhu, H.-J. Wang, M.-R. Gao, S.-H. Yu, *J. Am. Chem. Soc.* **2020**, *142*, 6400.

[8] T. T. H. Hoang, S. Verma, S. Ma, T. T. Fister, J. Timoshenko, A. I. Frenkel, P. J. A. Kenis, A. A. Gewirth, *J. Am. Chem. Soc.* **2018**, *140*, 5791.

[9] S. Ren, D. Joulie, D. Salvatore, K. Torbensen, M. Wang, M. Robert, C. P. Berlinguette, *Science* **2019**, *365*, 367.

[10] D. Gao, R. M. Arán-Ais, H. S. Jeon, B. Roldan Cuenya, *Nat. Catal.* **2019**, *2*, 198.

[11] Z. Gu, H. Shen, L. Shang, X. Lv, L. Qian, G. Zheng, *Small Methods* **2018**, *2*, 1800121.

[12] Y. Y. Birdja, E. Pérez-Gallent, M. C. Figueiredo, A. J. Göttle, F. Calle-Vallejo, M. T. M. Koper, *Nat. Energy* **2019**, *4*, 732.

[13] S. Popović, M. Smiljanić, P. Jovanovič, J. Vavra, R. Buonsanti, N. Hodnik, *Angew. Chem., Int. Ed.* **2020**, *59*, 14736.

[14] S. Nitopi, E. Bertheussen, S. B. Scott, X. Liu, A. K. Engstfeld, S. Horch, B. Seger, I. E. L. Stephens, K. Chan, C. Hahn, J. K. Nørskov, T. F. Jaramillo, I. Chorkendorff, *Chem. Rev.* **2019**, *119*, 7610.

[15] T.-T. Zhuang, Y. Pang, Z.-Q. Liang, Z. Wang, Y. Li, C.-S. Tan, J. Li, C. T. Dinh, P. De Luna, P.-L. Hsieh, T. Burdyny, H.-H. Li, M. Liu, Y. Wang, F. Li, A. Proppe, A. Johnston, D.-H. Nam, Z.-Y. Wu, Y.-R. Zheng, A. H. Ip, H. Tan, L.-J. Chen, S.-H. Yu, S. O. Kelley, D. Sinton, E. H. Sargent, *Nat. Catal.* **2018**, *1*, 946.

[16] C.-T. Dinh, T. Burdyny, M. G. Kibria, A. Seifitokaldani, C. M. Gabardo, F. P. G. de Arquer, A. Kiani, J. P. Edwards, P. De Luna, O. S. Bushuyev, C. Zou, R. Quintero-Bermudez, Y. Pang, D. Sinton, E. H. Sargent, *Science* **2018**, *360*, 783.

[17] D. Kim, C. S. Kley, Y. Li, P. Yang, *Proc. Natl. Acad. Sci.* **2017**, *114*, 10560.

[18] C. Chen, J. F. Khosrowabadi Kotyk, S. W. Sheehan, *Chem* **2018**, *4*, 2571.

[19] G. L. De Gregorio, T. Burdyny, A. Loiudice, P. Iyengar, W. A. Smith, R. Buonsanti, *ACS Catal.* **2020**, *10*, 4854.

[20] Y. Gao, Q. Wu, X. Liang, Z. Wang, Z. Zheng, P. Wang, Y. Liu, Y. Dai, M.-H. Whangbo, B. Huang, *Adv. Sci.* **2020**, *7*, 1902820.

[21] K. D. Yang, W. R. Ko, J. H. Lee, S. J. Kim, H. Lee, M. H. Lee, N. Ki Tae, *Angew. Chem., Int. Ed.* **2017**, *56*, 796.

[22] T.-T. Zhuang, Z.-Q. Liang, A. Seifitokaldani, Y. Li, P. De Luna, T. Burdyny, F. Che, F. Meng, Y. Min, R. Quintero-Bermudez, C. T. Dinh, Y. Pang, M. Zhong, B. Zhang, J. Li, P.-N. Chen, X.-L. Zheng, H. Liang, W.-N. Ge, B.-J. Ye, D. Sinton, S.-H. Yu, E. H. Sargent, *Nat. Catal.* **2018**, *1*, 421.

[23] G. Singh, J. Lee, A. Karakoti, R. Bahadur, J. Yi, D. Zhao, K. AlBahily, A. Vinu, *Chem. Soc. Rev.* **2020**, *49*, 4360.

[24] J. Liu, J. Fu, Y. Zhou, W. Zhu, L.-P. Jiang, Y. Lin, *Nano Lett.* **2020**, *20*, 4823.

[25] J.-R. Li, H.-C. Zhou, *Nat. Chem.* **2010**, *2*, 893.

[26] L.-B. Sun, J.-R. Li, W. Lu, Z.-Y. Gu, Z. Luo, H.-C. Zhou, *J. Am. Chem. Soc.* **2012**, *134*, 15923.

[27] Y. Chen, X. Feng, X. Huang, Z. Lin, X. Pei, S. Li, J. Li, S. Wang, R. Li, B. Wang, *Chem. Eur. J.* **2015**, *21*, 13894.

[28] J. F. Xu, W. Ji, Z. X. Shen, W. S. Li, S. H. Tang, X. R. Ye, D. Z. Jia, X. Q. Xin, *J. Raman Spectrosc.* **1999**, *30*, 413.

[29] Y.-R. Wang, R.-X. Yang, Y. Chen, G.-K. Gao, Y.-J. Wang, S.-L. Li, Y.-Q. Lan, *Sci. Bull.* **2020**, *65*, 1635.

[30] M. C. Biesinger, L. W. M. Lau, A. R. Gerson, R. S. C. Smart, *Appl. Surf. Sci.* **2010**, *257*, 887.

[31] W. Zhang, C. Huang, Q. Xiao, L. Yu, L. Shuai, P. An, J. Zhang, M. Qiu, Z. Ren, Y. Yu, *J. Am. Chem. Soc.* **2020**, *142*, 11417.

[32] P. Gaudin, P. Fioux, S. Dorge, H. Nouali, M. Vierling, E. Fiani, M. Molière, J.-F. Brilhac, J. Patarin, *Fuel Process. Technol.* **2016**, *153*, 129.

[33] Q. Zou, Y. Wei, S. Wang, J. Xie, A. Xu, X. Li, *Appl. Organomet. Chem.* **2019**, *33*, e4815.

[34] Y.-J. Tang, Y. Wang, H.-J. Zhu, K. Zhou, Y.-Q. Lan, *J. Mater. Chem. A* **2019**, *7*, 13559.

[35] E. Z. Kurmaev, V. R. Galakhov, V. V. Fedorenko, L. V. Elokhina, S. Bartkowski, M. Neumann, C. Greaves, P. P. Edwards, M. Al-Mamouri, D. L. Novikov, *Phys. Rev. B* **1995**, *52*, 2390.

[36] K. Chen, J.-L. Ling, C.-D. Wu, *Angew. Chem., Int. Ed.* **2020**, *59*, 1925.

[37] Q. Zhu, X. Sun, D. Yang, J. Ma, X. Kang, L. Zheng, J. Zhang, Z. Wu, B. Han, *Nat. Commun.* **2019**, *10*, 3851.

[38] J.-J. Lv, M. Jouny, W. Luc, W. Zhu, J.-J. Zhu, F. Jiao, *Adv. Mater.* **2018**, *30*, 1803111.

[39] J. Kim, W. Choi, J. W. Park, C. Kim, M. Kim, H. Song, *J. Am. Chem. Soc.* **2019**, *141*, 6986.

[40] H. Yang, Q. Lin, C. Zhang, X. Yu, Z. Cheng, G. Li, Q. Hu, X. Ren, Q. Zhang, J. Liu, C. He, *Nat. Commun.* **2020**, *11*, 593.

[41] L. Wang, W. Chen, D. Zhang, Y. Du, R. Amal, S. Qiao, J. Wu, Z. Yin, *Chem. Soc. Rev.* **2019**, *48*, 5310.

[42] D.-H. Nam, P. De Luna, A. Rosas-Hernández, A. Thevenon, F. Li, T. Agapie, J. C. Peters, O. Shekhah, M. Eddaoudi, E. H. Sargent, *Nat. Mater.* **2020**, *19*, 266.

[43] J. K. Nørskov, J. Rossmeisl, A. Logadottir, L. Lindqvist, J. R. Kitchin, T. Bligaard, H. Jónsson, *J. Phys. Chem. B* **2004**, *108*, 17886.

[44] A. A. Peterson, F. Abild-Pedersen, F. Studt, J. Rossmeisl, J. K. Nørskov, *Energy Environ. Sci.* **2010**, *3*, 1311.

[45] A. A. Peterson, J. K. Nørskov, *J. Phys. Chem. Lett.* **2012**, *3*, 251.